A large-area ceramic GEM neutron detector with high efficiency at CSNS

Xiao-Juan Zhou(周晓娟)[1,2,3], Jian-Rong Zhou(周健荣)[1,2,3*], Li-Xin Zeng(曾莉欣)[1,2], Fei Jia(贾飞)[1,2,4], Hong Xu(许虹)[1,2], Yuan-Guang Xia(夏远光)[1,2], Yi-Chao Ma(马毅超)[5], Chao-Yue Zhang(张超月)[1,2,4], Xing-Fen Jiang(蒋兴奋)[1,2], Hong-Yang Yin(尹弘扬)[1,2,6], Kai-Jun Chen(陈锴俊) [1,2,6], Yu-Guang Xie(谢宇广)[1], Yu-Bin Zhao(赵豫斌)[1,2], Jian Zhuang(庄建)[1,2], Zhi-Jia Sun(孙志嘉)[1,2,3], and Yuan-Bo Chen(陈元柏)[1,2,3]

[1]Institute of High Energy Physics, Chinese Academy of Sciences, Beijing 100049, China
[2]Spallation Neutron Source Science Center, Dongguan 523803, China
[3]University of Chinese Academy of Sciences, Beijing 100049, China
[4] College of Nuclear Science and Technology, Harbin Engineering University, Harbin 150000, China
[5] College of Electrical and Information Engineering of Shanxi University of Science and Technology, Xi'an 710021, China
[6]School of Nuclear Science and Technology, Lanzhou University, Lanzhou 730000, China

Abstract:

With the development of neutron sources towards higher fluxes, detectors require higher counting rates to remain applicable, especially for direct-beam or small-angle scattering measurements. Gas electron multiplier (GEM) detectors have emerged as a suitable candidate owing to their high counting rate capability, high spatial resolution, and feasibility for large-area fabrication. This paper presents a prototype multilayer boron-coated ceramic GEM detector developed at the China Spallation Neutron Source (CSNS). The ceramic GEM, originally developed by the Institute of High Energy Physics (IHEP), was employed to reduce neutron scattering owing to its high transmittance and low self-scattering. To date, a multilayer ceramic GEM detector has been fabricated and tested. The detector features an active area of 200.7 mm × 200.7 mm, a spatial resolution better than 2.5 mm (full width at half maximum, FWHM), a maximum system counting rate exceeding 1.1 MHz, and a neutron detection efficiency of approximately 43 ± 2% at a wavelength of 4.8 Å. Moreover, the detector exhibits good imaging capability and can be used for large-volume imaging. Its excellent performance makes it well suited for the Very Small Angle Neutron Scattering (VSANS) instrument and the Energy-resolved Neutron Imaging Instrument (ERNI) at CSNS.

Keywords: neutron detector, ceramic GEM, multilayer, high efficiency
PACS: 07.07.Df, 29.40.Gx, 28.20.Pr, 61.05.F–

*Corresponding author. E-mail: zhoujr@ihep.ac.cn

1. Introduction

As an ideal probe for studying the structure and dynamics of matter, neutron scattering has been widely applied in many fields. Compared with other techniques, neutron scattering has many irreplaceable advantages, such as strong penetrability, sensitivity to light elements, isotope discrimination, and magnetic microscopy capabilities. Consequently, scientists have recognized the pivotal role of spallation neutron sources—which can provide higher neutron flux and utilization efficiency—in modern science and technology. High-performance comprehensive experimental facilities for neutron science have been actively developed, and spallation sources with beam power in the megawatt range have been constructed. The peak neutron flux they produce is hundreds of times greater than that of reactors, providing a powerful platform for innovative research in materials science. At present, the main pulsed spallation neutron sources in operation worldwide include the Spallation Neutron Source (SNS) in the USA,[1] the ISIS Neutron and Muon Source (ISIS) in the UK,[2] the Japan Proton Accelerator Complex (J-PARC) in Japan,[3] the China Spallation Neutron Source (CSNS) in China,[4] and the European Spallation Source (ESS) in Europe. CSNS, the first spallation neutron source in a developing country, began construction in 2011 and successfully passed national acceptance in 2018. The first phase of the CSNS project mainly comprised one H^- linear accelerator, one rapid-cycling proton synchrotron, one target station, three spectrometers, and corresponding auxiliary facilities. In recent years, 11 neutron spectrometers have been developed. In 2024, the second phase of the CSNS project was launched: the accelerator target beam power will be increased to 500 kW, and nine new neutron spectrometers will be constructed concurrently. Currently, CSNS has achieved stable operation with a power of 185 kW and a pulse repetition rate of 25 Hz. With the advancement of new-generation neutron science facilities, the neutron beam flux continues to increase, creating an urgent demand for detectors with high counting rates and high resolution that are positioned close to the beam centre, such as those required for the Very Small Angle Neutron Scattering (VSANS) instrument, Multipurpose Reflectometer (MR), Liquids Neutron Reflectometer (LNR), and Energy-resolved Neutron Imaging Instrument (ERNI).

In the past few decades, ^{3}He-based multiwire proportional chambers (MWPCs) have been widely used owing to their high efficiency for thermal neutrons. However, limited by their intrinsic counting rate (<100 kHz), traditional wire-structured detectors can no longer meet the

requirements of high-throughput measurements. Over the past decade, scientists worldwide have been actively exploring new neutron detection technologies. The Gas Electron Multiplier (GEM), first developed by Sauli in 1997, is a novel type of gas detector that has been extensively developed in recent years, with its technology becoming increasingly mature.[5,6][5] Compared with traditional wire chambers, GEM detectors modify the electric field distribution in the working gas through a specially designed perforated conductive foil, thereby enhancing the electron amplification factor. GEM detectors offer strong performance: good spatial resolution, very high counting rate capability (~10 MHz), radiation resistance, flexible readout modes, and the feasibility of large-area fabrication at relatively low cost. When coupled with boron—an ideal thermal neutron conversion material, GEM detectors can be effectively applied to neutron detection. Around 2000, Schmidt and Klein at Heidelberg University in Germany first proposed the concept and basic structure of a GEM neutron detector based on a boron conversion layer. In 2004, they successfully developed the first small-area GEM neutron detector, named the GEM CASCADE detector, which employed several GEMs arranged in a cascaded configuration to increase detection efficiency.[7,8] In 2012, the Italian National Laboratory (INFN) developed a GEM-based thermal neutron beam monitor and successfully applied it at the ISIS spallation source on the VESUVIO beamline.[9-11] The aforementioned GEM detectors used standard GEM foils produced at CERN, which employ polyimide as the insulating layer. Additionally, the High Energy Accelerator Research Organization (KEK) in Japan developed a GEM neutron beam monitor and a multilayer GEM detector with an effective area of 100 mm × 100 mm around 2010, which were successfully deployed at J-PARC (NOVA).[12,13] The GEM foils used in these systems were LCP GEMs produced by a Japanese company, using liquid crystal polymer (LCP) as the insulator.

Given that neutrons are sensitive to hydrogen, in 2013, a unique ceramic GEM for neutron detection was proposed by IHEP and has since been successfully applied to neutron detection at CSNS. Owing to the use of ceramic as the insulating material, ceramic GEMs exhibit superior radiation resistance and stability, as well as reduced neutron self-absorption and self-scattering.[14-18] Ceramic GEM-based neutron detectors have been successfully deployed at CSNS as time-of-flight neutron beam monitors and have been operating stably for over eight years.[19-23] A prototype of a large-area, high-efficiency ceramic GEM neutron detector was

subsequently developed and tested, and has been adopted for use at VSANS and ERNI at CSNS.[24-26] This paper describes the performance and test results obtained at Beam Line 20 (BL20) at CSNS.

2. Detector principle

The ceramic GEM neutron detector features a symmetrical structure and consists of multilayer cascaded boron-coated ceramic GEM foils that serve both as neutron conversion carriers and as gas amplification elements. The information from neutron events is read out by the readout electrode. The detector can be divided into three mutually independent parts: neutron conversion, gas multiplication, and signal collection. The working gas is a mixture of Ne (97%) and iC_4H_{10} (3%), supplied in a continuous flow mode at atmospheric pressure to ensure detector stability and prolong its service life. The boron isotope ^{10}B is an ideal solid thermal neutron conversion material owing to its low chemical reactivity and the availability of highly enriched isotopes in large quantities. Neutrons interact with ^{10}B via the following reactions:

$n + {}^{10}B \rightarrow \alpha + {}^{7}Li + 2.79\ MeV$ 7% E_α=1.78 MeV, E_{Li}=1.0 MeV

$\rightarrow {}^{7}Li + \alpha + \gamma + 2.31\ MeV$ 93% E_α=1.47 MeV, E_{Li}=0.84 MeV

The ^{7}Li and alpha particles produced by these reactions interact with boron atoms through Coulomb interactions and gradually lose energy. Owing to the limited range of the ^{7}Li and alpha particles, increasing the thickness of a single boron layer beyond 3 μm does not improve the neutron conversion efficiency. To achieve high conversion efficiency, boron is coated on both the drift electrode and the GEM surfaces, and a multilayer laminated structure is employed. This configuration ensures that ^{7}Li and alpha particles can escape from the conversion layer and allows incident neutrons to pass through a sufficiently thick effective conversion volume. When an incident neutron is captured by boron, ^{7}Li and alpha particles are emitted in opposite directions. One of these particles is absorbed directly in the boron-coated substrate, while the other enters the working gas, producing numerous primary electron–ion pairs. Driven by the drift electric field, electrons traverse the drift region and pass through each layer of boron-coated GEM foil (with a gain of approximately 1), allowing the neutron interaction information carried by the primary electrons to pass through all conversion layers without distortion. Gas amplification is performed by the bottom-layer GEM foil (with a gain of several tens), and finally the neutron interaction position is determined by the two-dimensional readout structure, as shown in Fig. 1.

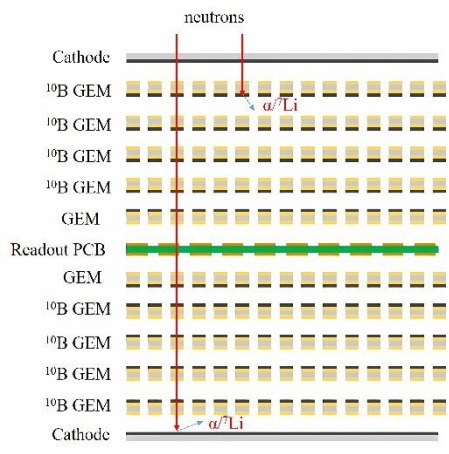


Fig. 1. Detector schematic.

Since the neutron beam intensity decreases exponentially with increasing thickness of the conversion layers, the total conversion efficiency does not increase linearly with the number of layers. When the number of layers reaches a certain value, the conversion efficiency tends to saturate. Based on Monte Carlo simulations of conversion efficiencies for different layer numbers and thicknesses, the detector employs two layers of B_4C cathode (a 0.1 mm $AlMg_3$ plate coated with a 1 μm layer of isotope-enriched $^{10}B_4C$, ^{10}B enrichment > 96%) and ten layers of single-side boron-coated ceramic GEM (ceramic GEM coated with 1.2 μm layer of isotope-enriched ^{10}B, ^{10}B enrichment > 96%) for neutron conversion. The boron-coated ceramic GEM layers that serve for neutron conversion without providing amplification are referred to as conversion-layer GEMs. The layer located adjacent to the two-dimensional readout circuit board, which serves both neutron conversion and gas amplification functions, is referred to as the amplification layer GEM. The electric field between the drift electrode and the first conversion layer GEM is defined as the drift electric field; the electric field between adjacent ceramic GEM layers is defined as the transfer electric field; and the electric field between the amplification layer GEM and the two-dimensional readout circuit board is defined as the collection (induction) electric field. Without reducing the number of boron-coated GEM layers (which would decrease conversion efficiency), a symmetrical installation of GEM detection units—comprising one B_4C cathode and five single-side boron-coated ceramic GEM layers on each side—is adopted. The readout electrode collects signals from both sides from the middle, which reduces the required high voltage by half.

3. Detector prototype

3.1 Ceramic GEM

Since neutrons are sensitive to hydrogen, they are easily scattered by hydrogen atoms, which degrades the spatial resolution and measurement accuracy of the detector. To reduce scattering between neutrons and the GEM foils, especially in the multilayer GEM structure with a total thickness of approximately 2 mm, IHEP developed a ceramic GEM whose neutron absorption is only half that of an FR4 GEM with the same dimensions,[14] making it well suited for neutron detection. The insulating substrate consists of 90% pure ceramic and 10% glass fibres. The main components of the ceramic GEM are oxygen, silicon and aluminium, with mass fractions of 48.5%, 34.3% and 8%, respectively, and the total neutron cross-sections of 3.98 barn, 2.20 barn and 1.69 barn, respectively. In contrast, the total neutron cross section of hydrogen is 30.6 barn, while hydrogen accounts for nearly 0% of all elements in the ceramic substrate. Therefore, the influence of the ceramic GEM itself on neutron detector performance is minimized. The ceramic GEM was manufactured cost-effectively using printed circuit board technology. The total thickness of the ceramic GEM is 200 μm, comprising a 170 μm ceramic substrate and 15 μm copper layers on both sides. Numerous holes are formed by mechanical drilling at a rate of 300 holes per minute (Fig. 2(a)). Each hole has a diameter of 200 μm, and the holes are distributed on a 600 μm pitch. An 80 μm rim is formed by Cu etching. The ceramic GEM subsequently undergoes cleaning, shaping, baking, and testing to obtain intact samples, as shown in Fig. 2(b). Currently, ceramic GEMs with an active area of 200 mm × 200 mm (nearly 128,000 holes) have been produced, with a hole precision of approximately ±25 μm and a yield exceeding 80%. To increase neutron conversion efficiency, a 1.2 μm layer of isotopic boron was coated on a single side of the ceramic GEM for neutron conversion.

(a)  (b) 

Fig. 2. (a) Mechanical drilling. (b) 200 mm × 200 mm ceramic GEM.

3.2 Detector design

The multilayer ceramic GEM detector is designed as a standalone block. The detector gas chamber consists of two chambers, an upper chamber and a lower chamber, each containing one B_4C cathode and five boron-coated ceramic GEM layers. For multilayer GEM stack structures, maintaining the flatness of the GEM foils and the uniformity of the interlayer spacing is crucial. To ensure accurate alignment between GEM foils, a ceramic substrate support frame is placed between each layer. All support frames are fabricated using high-precision digital machine tools, with a flatness better than 0.1 mm and a machining accuracy exceeding 0.1 mm, ensuring precise installation and positioning of each foil. The ceramic substrate support frame is 2 mm thick, with grooves formed in the frame to provide support and facilitate gas flow. The gap dimensions of the drift gap, transfer gap and induction gap are all 2 mm. The upper and lower chambers are separated by a two-dimensional readout circuit board and sealed with O-rings. Currently, the commonly used signal readout methods include two-dimensional strip readout, in which the ionization point position is determined by calculating the centre of gravity of the charge, or two-dimensional signal matching methods to determine the ionization point position. Both methods employ a two-dimensional strip readout structure, use the same number of electronic circuits and operate within the same achievable range. Owing to the different readout methods, the former provides higher positioning accuracy but requires charge measurement, resulting in a lower readout speed than the latter. The latter uses a digital readout with a higher counting rate. Therefore, a two-dimensional signal matching method was chosen to determine the neutron hit position and achieve high counting rate performance. The two-dimensional readout circuit board is fabricated from flexible Kapton material with a total thickness of 0.8 mm to minimize neutron scattering, and the pixel size is 0.82 mm. To achieve consistency between the readout strips in both the X and the Y direction, each one-dimensional readout strip is connected by 256 triangular pads through PCB interlayer wiring, and the other side is designed to be completely symmetrical. The upper and lower symmetrical readout strips are directly connected to share a channel, and signal extraction is achieved through multilayer interlayer wiring. The readout board adopts multilayer wiring; to avoid crosstalk between signal lines, a shielding layer is added between every two wiring layers. The high-voltage distribution board, front-end ASICs, and data acquisition board are mounted directly on the back of the device (see Fig. 3) to improve system

integration. A resistor chain is used to apply different high voltages to different sections of the detector. To reduce neutron scattering and activation, the detector's mechanical parts are primarily made of aluminium alloy, and the neutron entrance window is 1 mm thick. In addition, neutron shielding has been carefully implemented: 2 mm thick boron-aluminium alloy plates are installed around the detector and at the bottom of the gas chamber to prevent direct neutron beam irradiation of the electronics. The detector operates in flowing gas mode at atmospheric pressure to avoid ageing effects.

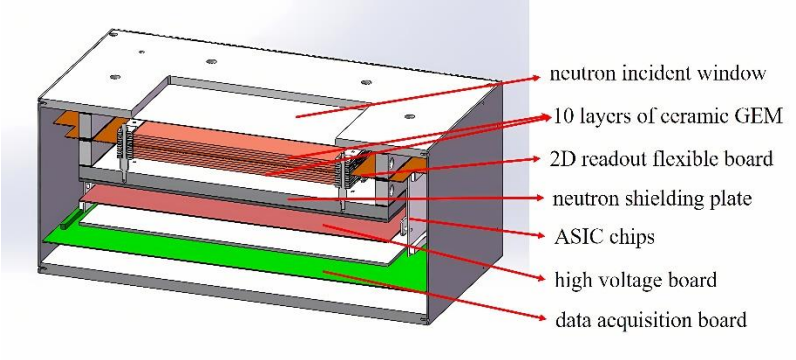


Fig. 3. Detector structure.

3.3 Detector assembly

Before assembly, each boron-coated ceramic GEM foil must undergo high-voltage testing in the working gas to ensure normal operation. Subsequently, performance testing was conducted using a ^{241}Am α source to obtain the gain versus high-voltage curve, which serves as the basis for selecting high-voltage distribution resistors on the high-voltage distribution board. During assembly, the lower chamber of the detector was installed first. One cathode layer, five boron-coated ceramic GEM layers, and ceramic support frames were installed sequentially. Notably, for four of the boron-coated ceramic GEM layers, the boron-coated surface faces the readout board; for the boron-coated ceramic GEM layer nearest the readout board, the boron-coated surface faces away from the readout board so that it can be amplified by the strong electric field in the hole. Afterwards, the two-dimensional readout circuit board was installed, and then the upper chamber was installed following the same procedure as for the lower chamber. The ASIC chip reads signals through ERNI connectors, and a shielding cover was installed over the ASIC chip to reduce interference. The detector adopts a resistor chain method, which provides multiple high voltages to the symmetrical ceramic GEMs through a single high-voltage channel. The resistances of the corresponding drift region, transfer region, induction region, conversion

layer ceramic GEM and amplification layer ceramic GEM are 6.8 M, 6.8 M, 10 M, 4.6 M, and 6.8 M, respectively. Under normal operating conditions, the applied high voltage is 2600 V, corresponding to a drift electric field strength of 1.3 kV/cm, a transfer electric field strength of 1.3 kV/cm, an induction electric field strength of 1.9 kV/cm, a conversion layer ceramic GEM gain of 1.4, and an amplification layer GEM gain of 17.8. A photograph of the detector is shown in Fig. 4.

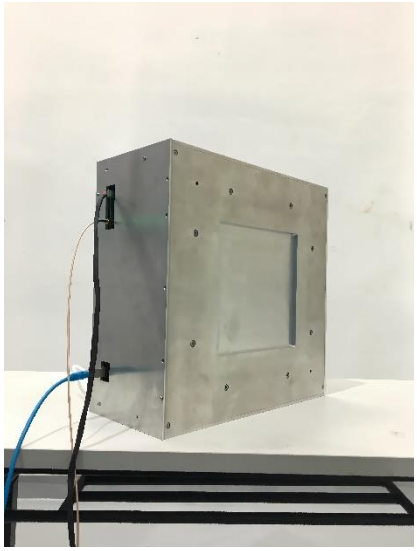


Fig. 4. Photograph of the detector.

3.4 Readout electronics and data acquisition system

High counting rate is the most significant advantage of GEM detectors. To meet the application requirements of the detector, a 512-channel high counting rate readout electronics system has been developed. The front-end readout circuit uses the AS20Board chip developed by the CASCADE group at the University of Heidelberg in Germany to perform analogue sampling, signal amplification, filtering and shaping of the detector output signals. The chip integrates 64 low-noise charge-sensitive preamplifier channels, with a maximum trigger rate of 10 MHz and a readout clock frequency of 40 MHz. During each readout clock cycle, signals from 16 channels are transmitted, and one complete triggered data transmission cycle is completed over four readout clock cycles. To meet the readout requirements of 512 channels, eight AS20Board front-end readout circuits are used.

To improve the efficiency of system signal analysis and data processing, the FPGA employs a pipelined architecture. The FPGA logic block diagram is shown in Figure 5. To meet the requirements for multichannel interface, high-speed data analysis and data transmission/reception,

the FPGA uses a XC7K-325TFBG676 chip from the Kintex-7 series as the main control chip. The abundant on-chip resources of this device satisfy the requirements for system resource configuration and data logic analysis. First, the FPGA configures the ASIC circuits via an I2C interface. Subsequently, signals are read from each ASIC over four consecutive 40 MHz readout clock cycles according to the control signal output by the AS20Board, and the 64-channel signals from each ASIC are recombined. Finally, data analysis is performed in the X/Y direction: eight groups of 64-channel signal data are combined to obtain 256 channels in each of the X and Y directions.

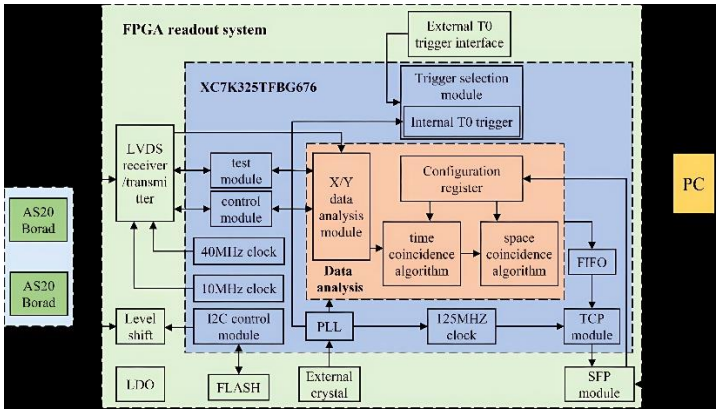


Fig. 5. FPGA logic block diagram.

To extract valid neutron event information, time coincidence analysis and space coincidence analysis are applied during data processing. Time coincidence analysis is required because the neutron signal duration is relatively long (usually between 200 and 300 ns) and can easily exceed the integration time of the comparator in the front-end circuit. Under these conditions, multiple triggers may occur at the same position within a short time. Therefore, the time coincidence algorithm treats neutron signals triggered multiple times within the coincidence time window as a single neutron signal and filters out redundant trigger signals. Spatial coincidence analysis is performed because, among the 256 channel signals in the X and Y directions, multiple channels may simultaneously contain signals. When signals appear in multiple continuous channels, the FPGA adopts a centroiding method for merging; when signals appear in multiple discontinuous channels simultaneously, these cases are handled as exceptions. The effective neutron events obtained through time and space coincidence analysis correspond to the two-dimensional coordinates of the neutron hit reconstructed from the X and Y readout strips. Then, neutron events (X, Y, T) are formed by adding a timestamp relative to each T0 using a clock. Finally, the neutron

events are stored in a FIFO by the FPGA and uploaded to a computer via the TCP/IP protocol.

4 Results and discussion

To evaluate the detector performance, a detailed experimental study was conducted at BL20 of CSNS, including measurements of neutron imaging performance, wavelength spectrum, counting rate capability, spatial resolution and detection efficiency. BL20 employs a decoupled and poisoned hydrogen moderator (DPHM) to provide neutron beams with different time pulse structures and neutron wavelength ranges.

4.1 Neutron imaging and wavelength spectrum

First, to verify that the multilayer boron-coated ceramic GEM detector system operates properly, beam imaging and wavelength spectra were measured using the time-of-flight (TOF) method. The distance between the beam exit port and the detector was 4.38 m. During testing, a Φ5 mm beam limiting aperture was placed in front of the detector. The image of the beam profile, which is consistent with the size of the neutron beam considering neutron divergence, is shown in Fig. 6(a), indicating that the neutron beam distribution is uniform. Furthermore, the wavelength spectrum distribution was obtained from the TOF distribution, as shown in Fig. 6(b). Two distinct Bragg edges are observed at 4.05 Å and 4.68 Å, corresponding to the Al(200) and Al(111) crystal planes, respectively, originating from neutron interactions with the aluminium components of the moderator and detector. These results demonstrate that the multilayer boron-coated ceramic GEM detector has excellent neutron imaging capability and can accurately measure the neutron wavelengths using TOF information. To evaluate detector uniformity, detailed tests were conducted. The detector was placed on a movable platform, with a 10 mm diameter boron-aluminium alloy beam limiting aperture at the front end. The effective area of the detector was divided into 3 × 3 regions. By moving the detector, neutron counts from each region were tested separately at the same time, and an LND beam monitor was used to normalize the beam flux fluctuations in each region. The relative standard deviation (RSD) of the nine regions obtained from the test is 4.3%, indicating good uniformity across the 200 mm × 200 mm effective area. In addition, to accurately measure the effective detector area, the detector was placed on a high-precision moving platform capable of left–right movement. The detector was moved by the platform while scanning the beam spot. The maximum detection displacement differences in the X and Y directions are 200.7 mm and 200.7 mm, respectively, indicating that the effective area of the

detector is 200.7 mm × 200.7 mm.

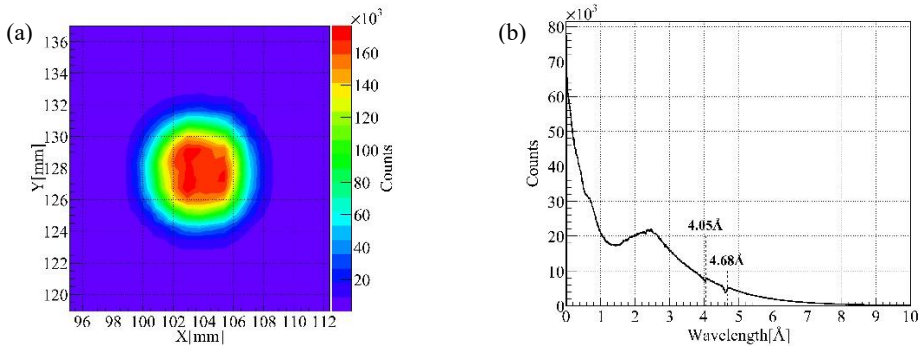


Fig. 6. (a) Beam imaging and (b) neutron wavelength spectrum.

4.2 Counting rate capability

The counting rate capacity of the system is a critical specification for detectors, given that high counting rate is the most significant advantage of GEM detectors, and the detector is intended for use on high-flux instruments. The counting rate capability was evaluated at BL20 of CSNS. During testing, the beam power was 100 kW and the beam spot size was Φ 10 mm. Since the neutron beam at CSNS operates in a pulsed mode with a frequency of 25Hz, the number of neutrons reaching the detector varies at different times within one pulse cycle. The test method is as follows: the detector faces the beam exit, and the TOF spectrum is measured. After the count in each channel of the TOF spectrum is divided by the effective pulse number and the time bin width, the instantaneous counting rate spectrum is obtained, from which the highest counting rate of the detector system can be read. The maximum counting rate of the multilayer boron-coated ceramic GEM detector exceeds 1.1 MHz.

4.3 Spatial resolution

Spatial resolution, usually defined as the full width at half maximum (FWHM) of a peak, is among the most essential parameters for a 2D position-sensitive detector and can be obtained by Gaussian fitting of the projected position distribution. To measure the spatial resolution, a 2 mm thick cadmium plate with three slits of 0.5 mm width each at a pitch of 50 mm was placed in front of the detector. By rotating the cadmium plate by 90 degrees, the spatial resolution in the X and Y directions could be measured separately. As shown in Fig. 7, the spatial resolutions in the X direction and Y direction are 2.4 ± 0.1 mm, 2.4 ± 0.1 mm, and 2.3 ± 0.1 mm and 2.4 ± 0.1 mm, 2.3 ± 0.1 mm, and 2.3 ± 0.1 mm (FWHM), respectively. The uncertainty of position resolution measurements mainly arises from statistical errors and systematic uncertainties, such as alignment

accuracy and beam divergence. To reduce systematic uncertainties, before measurement, a laser level was used to ensure that the neutron beam axis was precisely aligned and coplanar with the centre of the slit, minimizing systematic error caused by mechanical misalignment. During the experiment, the sensitive area of the detector outside the measurement region (i.e., outside the slits) was shielded with a cadmium plate, effectively preventing beam divergence from affecting the measurement results. Regarding statistical errors, the counts within the effective area for all measurements exceeded 10000, ensuring that the relative statistical error due to Poisson fluctuations was less than 1%.

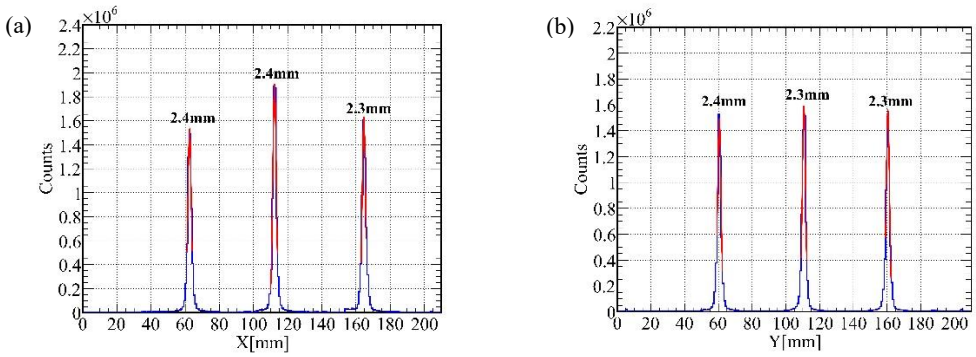


Fig. 7. Spatial resolutions in the X direction (a) and Y direction (b).

4.4 Detection efficiency

As described in Section 2, two B_4C cathode layers and ten boron-coated ceramic GEM layers were used to increase the detection efficiency. The detection efficiency was determined by comparison with the counts measured by a standard ^{3}He tube (LND252299, 1 inch in diameter, 20 atm) under the same conditions. During testing, a low-pressure ^{3}He beam monitor (Ordela 4560N) was placed at the beam exit port to monitor neutron beam intensity fluctuations so that subsequent data processing could be normalized to eliminate this interference. For the standard ^{3}He tube, the detection efficiency at the centre was close to 100% for cold neutrons. To increase the measurement accuracy, the ^{3}He tube was placed in a shielding box with a 1 mm diameter aperture, and its centre was aligned with the aperture to ensure that monochromatic neutrons entering the aperture could be detected with 100% efficiency. The standard ^{3}He tube with the neutron path stationary was then removed, and the response of neutrons passing through the aperture in the GEM detector was tested. In addition, the background of the detector was subtracted to further improve measurement accuracy. The detection efficiency (η) was calculated using the following

formula:

$$\eta = \frac{\frac{\varphi_{GEM}}{\varphi_{GEM_M}} - \frac{\varphi_{GEM_BG}}{\varphi_{GEM_M}}}{\frac{\varphi_{3He}}{\varphi_{3He_M}} - \frac{\varphi_{3He_BG}}{\varphi_{3He_M}}}$$

where φ_{GEM} / φ_{GEM_BG} represent the test and background counts of the multilayer boron-coated ceramic GEM detector, respectively; φ_{3He} / φ_{3He_BG} represent the test and background counts of the standard ^{3}He tube, respectively; and φ_{GEM_M} and φ_{3He_M} represent the counts of the beam monitor under the corresponding testing conditions.

During testing, the low-pressure ^{3}He beam monitor, a mica monochromator, the standard ^{3}He tube, and the multilayer boron-coated ceramic GEM detector were sequentially placed at the beam exit. Based on the neutron time-of-flight spectrum measured by the standard ^{3}He tube, φ_{3He} and φ_{3He_BG} were obtained. Next, keeping the experimental conditions unchanged, the standard ^{3}He tube was removed from the beam path, and testing of the multilayer boron-coated ceramic GEM detector commenced, yielding φ_{GEM} and φ_{GEM_BG}. Through calculation, the detection efficiency is 43±2% for neutrons with a wavelength of 4.8 Å. A comparison between the experimental results and the Geant4 simulation results is shown in Fig. 8. The simulated efficiency at 4.8 Å is 44%, which is consistent with the experimental results. The deviation in efficiency mainly arises from the angle deviation of the 1 mm aperture (±1.0%) and the wall absorption of the ^{3}He tube (±1.0%).

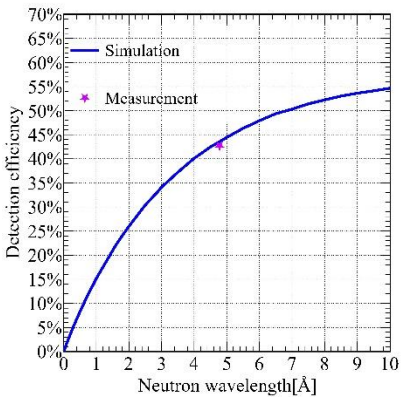


Fig. 8. Detection efficiency vs. neutron wavelength obtained by Geant4 simulation (curve) and experimental data (dotted dots).

5 Conclusion and outlook

Faced with the high-throughput neutron measurement requirements of spectrometers, a GEM neutron detector with the advantage of high counting rate was developed. A prototype multilayer

ceramic GEM neutron detector with two B_4C cathode layers and ten boron-coated ceramic GEM layers was developed at CSNS. The detector features an active area of 200.7 mm × 200.7 mm, a spatial resolution better than 2.5 mm (FWHM), a neutron detection efficiency of 43±2% at a wavelength of 4.8 Å, and a maximum system counting rate exceeding 1.1 MHz. Moreover, the detector is capable of measuring wavelength spectra and exhibits good imaging performance. The results indicate that the detector is highly suitable for direct-beam and near-beam measurements. In accordance with the detector design, dedicated detectors have been developed for VSANS and ERNI, and they have been running stably for over two years, providing users with high-quality data. To develop larger-area neutron detectors, we are currently investigating more advanced ceramic GEM manufacturing technologies, primarily focusing on laser drilling technology. By leveraging its advantages of micrometre-level positioning accuracy, fast drilling speed of up to 20000 holes/min, and noncontact processing, we aim to realize high-performance, metre-level ceramic GEM detectors.

Acknowledgements

This work was supported by the National Key R&D Program of China (Grant No. 2023YFC2206500), the National Natural Science Foundation of China (Grant No. 12227810, 12305208 and 12505351), Guangdong Major Project of Basic and Applied Basic Research (Grant No. 2023B0303000003), Guangdong Provincial Key Laboratory of Advanced Particle Detection Technology (Grant No. 2024B1212010005), Guangdong Basic and Applied Basic Research Foundation (Grant No. 2024B1515120006), and Songshan Lake High-tech Zone Joint Training Program for Engineering Master's and Doctoral Degrees.

References

[1] Mason T E, Abernathy D, Anderson I, Ankner J, Egami T, Ehlers G, Ekkebus A, Granroth G, Hagen M, Herwig K, Hodges J, Hoffmann C, Horak C, Horton L, Klose F, Larese J, Mesecar A, Myles D, Neuefeind J, Ohl M, Tulk C, Wang X L and Zhao J 2006 *Physica B* **385** 955

[2] Thomason J W 2019 *Nucl. Instrum. Methods Phys. Res. A* **917** 61

[3] Oyama Y 2006 *Nucl. Instrum. Methods Phys. Res. A* **562** 548

[4] Chen H S, Chen Y B, Fu S N, Ma L, Wang S, Chen F Q, Chen Y W, Dong H Y, Dong L, Feng

G, Gu J, He L H, He K, He W, Hu C M, Huang J S, Ji Q, Jia X J, Jin D P, Kang L, Kang W, Liang T J, Lin G P, Liu H C, Li J, Ouyang H F, Qi F Z, Qi X, Qu H M, Sun H, Sun Z J, Shen L, Tang J Y, Tao J Z, Wang F W, Wang L S, Wang P, Wang Q B, Wu Y Q, Xi J W, Xu T G, Yin W, Zhang B Y, Zhang J, Zhang J R, Zhang S Y, Zhao J S, Zhao L Y, Zhao Y B, Zhou M, Zhu T and Zhuang J 2025 *Nucl. Instrum. Methods Phys. Res. A* **1078** 170431

[5] Sauli F 1997 *Nucl. Instrum. Methods Phys. Res. A* **386** 531

[6] Sauli F 2016 *Nucl. Instrum. Methods Phys. Res. A* **805** 2

[7] Klein M and Schmidt C J 2011 *Nucl. Instrum. Methods Phys. Res. A* **628** 9

[8] Schmidt C J and Klein M 2006 *Neutron News* **17** 12

[9] Albani G, Croci G, Cazzaniga C, Cavenago M, Claps G, Muraro A, Murtas F, Pasqualotto R, Perelli Cippo E, Rebai M, Tardocchi M and Gorini G 2015 *J. Instrum.* **10** C04040

[10] Murtas F, Croci G, Claps G, Cavenago M, Dalla Palma M, Gervasini G, Grosso G, Pasqualotto R, Perelli Cippo E, Rebai M, Tardocchi M, Tollin M and Gorini G 2011 *2011 IEEE Nuclear Science Symposium Conference Record, October 23-29, 2011, Valencia, Spain, p. 405*

[11] Croci G, Claps G, Caniello R, Cazzaniga C, Grosso G, Murtas F, Tardocchi M, Vassallo E, Gorini G, Horstmann C, Kampmann R, Nowak G and Stoermer M 2013 *Nucl. Instrum. Methods Phys. Res. A* **732** 217

[12] Uno S, Uchida T, Sekimoto M, Murakami T, Miyama K, Shoji M, Nakano E, Koike T, Morita K, Satoh H, Kamiyama T and Kiyanagi Y 2012 *Phys. Procedia* **26** 142

[13] Uno S, Uchida T, Sekimoto M, Murakami T, Miyama K, Shoji M, Nakano E and Koike T 2012 *Phys. Procedia* **37** 600

[14] Zhou J R, Zhou X J, Zhou J J, Jiang X F, Yang J Q, Zhu L, Yang W Q, Yang T, Xu H, Xia Y G, Yang G A, Xie Y G, Huang C Q, Hu B T, Sun Z J and Chen Y B 2020 *Nucl. Eng. Technol.* **52** 1277

[15] Cancelli S, Muraro A, Perelli Cippo E, Romanelli G, Abba A, Chen Y B, Grosso G, Gorini G, Hu Z M, Lai C C, McCormack O, Robinson L, Svensson P O, Tardocchi M, Hall-Wilton R, Xie Y G, Sun Z J, Zhou J R, Zhou X J and Croci G 2021 *J. Instrum.* **16** P06003

[16] Hu Z M, Muraro A, Croci G, McCormack O, Perelli Cippo E, Tardocchi M, Zhou X J, Sun Z J, Zhou J R, Xie Y G, Chen Y B, Fan T S and Gorini G 2021 *Nucl. Instrum. Methods Phys. Res. A* **988** 164907

[17] Hu Z M, Muraro A, Gorini G, McCormack O, Perelli Cippo E, Tardocchi M, Sun Z J, Zhou X J, Zhou J R, Xie Y G, Chen Y B, Zhang H, Fan T S and Croci G 2022 *Nucl. Instrum. Methods Phys. Res. A* **1034** 166824

[18] Zhou J J, Zhou J R, Zhou X J, Zhu L, Yang W Q, Xu H, Guan B J, Wang S L, Yang J Q, Yang G A, Xie Y G, Zhang Y, Ding B W, Hu B T, Sun Z J, Duan L M and Chen Y B 2022 *Nucl. Instrum. Methods Phys. Res. A* **1024** 166076

[19] Zhou J R, Zhou X J, Zhou J J, Teng H Y, Yang J Q, Ma Y C, Zhou K, Xia Y G, Xiu Q L, Yang T, Jiang X F, Zhu L, Yang W Q, Yang G A, Xie Y G, Hu B T, Sun Z J and Chen Y B 2020 *Nucl. Instrum. Methods Phys. Res. A* **962** 163593

[20] Yang T, Zhou J R, Zhou X J, Zhu L, Zhu H Y, Zhou J J, Xia Y G, Wei Y D, Jiang X F, Yang W Q, Yang G A, Wang S L, Xie Y G, Sun Z J, Ouyang Q, Zhu J T and Chen Y B 2022 *IEEE Trans. Nucl. Sci.* **69** 68

[21] Zhu L, Zhou J R, Zeng L X, Xiao L, Zhou X J, Tan J H, Xia Y G, Xu H, Jiang X F, Yang W Q, Wang Y F, Yang G A, Xie Y G, Teng H Y, Li J J, Qiu Y X, Shen P X, Wang S L, Zhuang J, Zhao Y B, Zhang J R, Sun Z J and Chen Y B 2023 *J. Instrum.* **18** P01033

[22] Tan J H, Zhou J R, Zhu L, Zhou X J, Zeng L X, Xiao L, Xia Y G, Xu H, Jiang X F, Yang W Q, Wang Y F, Yang G A, Xie Y G, Teng H Y, Li J J, Qiu Y X, Shen P X, Wang S L, Liu Y, Zhu J T, Zhuang J, Zhao Y B, Sun Z J, Song Y S and Chen Y B 2023 *Rev. Sci. Instrum.* **94** 103304

[23] Zhu L, Zhou J R, Zhou X J, Zeng L X, Xiao L, Xu H, Jia F, Zhang C Y, Jiang X F, Wang Y F, Xie Y G, Fan R R, Zhao Y B, Sun Z J and Chen Y B 2025 *J. Instrum.* **20** P10050

[24] Zuo T S, Han Z H, Ma C L, Xiao S W, Lin X, Li Y Q, Wang F W, He Y C, He Z Q, Zhang J S, Wang G Y and Cheng H 2024 *J. Appl. Crystallogr.* **57** 380

[25] Zhang C Y, Zhou J R, Song Y S, Zhou X J, Jia F, Zeng L X, Yang W Q, Jiang X F, Xie Y G, Wang S L, Wang Y F, Zhao Y B, Zhuang J, Sun Z J and Chen Y B 2025 *J. Instrum.* **20** P12029

[26] Zhu L, Zhou J R, Zhou X J, Zeng L X, Xiao L, Xu H, Jia F, Zhang C Y, Yang Y Z, Li D F, Xiong H, Xie Y G, Zhao Y B, Wei Y D, Sun Z J and Chen Y B 2025 *Chin. Phys. B* **34** 090701